

Order-by-disorder without quantum zero-point fluctuations in the pyrochlore Heisenberg ferromagnet with Dzyaloshinskii-Moriya interactions

Alexander Hickey,^{1,*} Daniel Lozano-Gómez,^{1,2,3,*} and Michel J. P. Gingras¹

¹*Department of Physics and Astronomy, University of Waterloo, Waterloo, Ontario N2L 3G1, Canada*

²*Institut für Theoretische Physik and Würzburg-Dresden Cluster of Excellence ct.qmat*

³*Technische Universität Dresden, 01062 Dresden, Germany*

(Dated: March 6, 2024)

Order-by-disorder, whereby fluctuations lift an accidental classical ground state degeneracy to stabilize a subset of ordered states, is a recurrent and prominent theme in the field of frustrated magnetism where magnetic moments, or spins, are subject to competing interactions. Thus far, such a phenomenon has been discussed in systems where the quantum ground state is not a product state. In this circumstance, both thermal and quantum fluctuations act to lift the accidental classical degeneracy, begging the question whether one mechanism of order-by-disorder is possible without the other. In this paper, we present results exposing a novel route to order-by-disorder, without quantum zero-point fluctuations, in a family of ferromagnetic Heisenberg materials with the Dzyaloshinskii-Moriya (DM) interaction as the leading perturbation. We prove that any collinear ferromagnetic state is an *exact* eigenstate, even in the presence of the anisotropic DM interaction, while thermal fluctuations give rise to a preference in the magnetization direction. Here, we present in detail an example of the pyrochlore Heisenberg ferromagnet with DM interactions. Using both linear spin-wave theory and classical Monte Carlo simulations, we find that the magnetization can spontaneously rotate at intermediate temperature(s) within the collinear ferromagnetic phase when the DM interaction is large. Additionally, we find that in the large DM regime, the ferromagnetic ground state becomes unstable within the framework of non-linear spin-wave theory. Our results show that thermal order-by-disorder is possible even in the absence of quantum zero-point fluctuations.

I. INTRODUCTION

In correlated many-body systems with competing or frustrated interactions, thermal and quantum fluctuations may suppress the development of a symmetry-breaking transition to long-range order down to extremely low temperatures and, in some cases, completely prevent it [1–9]. This observation, however, does not mean that the presence of such fluctuations only has the effect of undermining the development of long-range ordered phases. Indeed, a contrary and at first sight seemingly paradoxical scenario may arise where the long-range order can be *assisted* by the presence of quantum or thermal fluctuations, a phenomenon known as *order-by-disorder* (ObD) [10–12]. In this context, the study of frustrated magnetic systems has proven to be fruitful ground in the study and realization of this phenomenon, where competing exchange interactions result in a set of “accidentally” degenerate ground-state configurations at the classical level that are not protected by symmetries of the Hamiltonian [13–15]. Thanks to the lack of any symmetry protecting this ground state degeneracy, the system becomes prone to selecting a subset of configurations within the degenerate manifold of classical ground states due to spin fluctuations. These fluctuations can be both thermal ($T > 0$) or quantum ($T = 0$) in origin. In the thermal case, a subset of the degenerate states are selected by maximizing the entropy associated with fluctuating about the “selected” ordered magnetic moment [16]. Conversely, the lifting of degeneracy at the quantum level occurs as a result of perturbative corrections to the ground state energy, relative to the classical model, from an inherently semi-classical description of a quantum many-body system

[17] — the true ground state of the quantum model not having a degeneracy to lift in the first place.

Despite the distinction between thermal and quantum fluctuations, both of these routes to fluctuation-induced selection are referred to colloquially as ObD [18–20]. Over the last several decades, there has been a large body of theoretical work focusing on models which exhibit thermal ObD [11, 15, 16, 18, 20–26] and quantum ObD [12, 13, 19, 27–45]. In this context, it has been commonplace in the literature to focus on a single mechanism of fluctuations, either thermal *or* quantum. While it is often the case that both quantum and thermal fluctuations select the same configurations [14], these two mechanisms of fluctuations may instead favor *distinct* long-range order, resulting in an additional transition between two ordered states at $T < T_c$, where T_c is the paramagnetic critical temperature [26, 46–49]. This implies that both thermal and quantum fluctuations must be accounted for to obtain a comprehensive understanding of the selected ordered phases at finite temperature. We note that the lifting of degeneracy due to quenched random disorder can also be referred to as ObD [1, 14, 50–55]. This is, however, a distinct physical mechanism that is not considered in this paper. While theoretical work is abundant on ObD for specific spin models, there is only a handful of real materials in which strong experimental signatures of ObD exist. The most prominent examples of such an ObD selection have been compellingly demonstrated in the compounds $\text{Er}_2\text{Ti}_2\text{O}_7$ [38, 39, 56, 57], [58], CoTiO_3 [59], $\text{Sr}_2\text{Cu}_3\text{O}_4\text{Cl}_2$ [60], $\text{Fe}_2\text{Ca}_3(\text{GeO}_4)_3$ [61] and $\text{Yb}_2\text{Ge}_2\text{O}_7$ [62].

To the best of our knowledge, all known examples of ObD selection in magnetic systems thus far exhibit both quantum ($T = 0$) and thermal ($T > 0$) ObD. Naturally, this leads to a fundamental question surrounding our current framework for understanding ObD: does the existence of thermal ObD *necessarily* imply the existence of quantum ObD? That is, can

* These authors contributed equally to the project.

we have one without the other? In the present work, we address this question by studying the ferromagnetic pyrochlore Heisenberg model with an additional anisotropic Dzyaloshinskii–Moriya (DM) interaction as the leading perturbation. In particular, we present the completely worked out example of ObD on the pyrochlore lattice with nearest-neighbor DM interactions. For a wide range of parameters, the ground state of this Hamiltonian is a uniform colinear ferromagnet with an accidental $O(3)$ degeneracy. We show that this system displays a *purely* thermal ObD selection, while quantum ObD selection is *absent* at zero-temperature, implying that thermal ObD can exist independently of quantum ObD in a magnetic quantum material. We investigate how the ground state degeneracy is lifted due to thermal fluctuations, using both classical and quantum methods, to provide insight on the order parameter selection at all temperatures within the ordered phase. The results pertaining to this spin model therefore represents a first realization of a system exhibiting ObD in the absence of zero-point fluctuations. Additionally, we analyze the stability of the ferromagnetic order in the quantum limit for an $S = \frac{1}{2}$ system using non-linear spin-wave theory, identifying a region of instability of the ferromagnetic order which was first alluded to in a very recent work [49]. While the results presented here are specifically for the pyrochlore lattice, we propose that the same qualitative effects should arise in any Heisenberg ferromagnet with DM interactions as long as the sum of the DM vectors along the bonds surrounding each site vanishes.

II. MODEL

We consider the Heisenberg and Dzyaloshinskii–Moriya (DM) Hamiltonian on the pyrochlore lattice, described by the Hamiltonian

$$\mathcal{H} = -J \sum_{\langle i,j \rangle} \mathbf{S}_i \cdot \mathbf{S}_j + D \sum_{\langle i,j \rangle} \mathbf{d}_{ij} \cdot (\mathbf{S}_i \times \mathbf{S}_j), \quad (1)$$

where $\langle i, j \rangle$ refers to the sum over all nearest-neighbor sites, $J > 0$ is the ferromagnetic Heisenberg coupling [63], and $\{\mathbf{d}_{ij}\}$ are the nearest-neighbor DM vectors determined by the Moriya rules [64] and listed in Appendix A. This choice of the DM vectors are referred to as being indirect (direct) [22] when $D > 0$ ($D < 0$).

Classically, the ground states of this model are magnetically ordered phases with $\mathbf{q} = \mathbf{0}$ ordering wavevector [65], i.e. the magnetic order is fully determined by a spin configuration of a single tetrahedron. The classical ground state configurations are determined by expressing Eq. (1) as a sum of single tetrahedra, $\mathcal{H} = \sum_{\mathbb{T}} \mathcal{H}^{\mathbb{T}}$, and then minimizing the resulting single-tetrahedron Hamiltonian $\mathcal{H}^{\mathbb{T}}$. The result of this calculation is pictorially illustrated in Fig. 1, where three distinct sets of classical spin configurations are identified: the “all-in-all-out” antiferromagnetic states for $D/J < -1$, colinear ferromagnetic configurations for $-1 < \frac{D}{J} < 2$, and the antiferromagnetic “ T_5 ” configurations for $D/J > 2$ [22, 24, 49].

It is already known that the Γ_5 region of the phase diagram exhibits an accidental ground state degeneracy at the classical level, parameterized by the global rotation group $O(2)$ [65].

This continuous symmetry group is reduced by both thermal and quantum fluctuations, resulting in six degenerate ordered configurations that are related by local discrete rotation about a local z axis [22, 24, 49]. Here, we point out that the ferromagnetic regime ($-1 < \frac{D}{J} < 2$) of Eq. (1) also exhibits and accidental ground state degeneracy at the classical level whenever $D \neq 0$. Inspecting each term in Eq. (1), we see that the Heisenberg exchange is completely isotropic, while the cross product appearing in the DM interaction obviously vanishes for any perfectly colinear configuration. This implies that the different ferromagnetic ground states are related by rotations in three-dimensional space, and can be parametrized by the continuous rotation group $O(3)$. This degeneracy of the classical ground state is accidental, as Eq. (1) has no continuous symmetry [66]. Naively, one might expect this accidental degeneracy to be lifted by both quantum and thermal fluctuations, selecting a subset of the ferromagnetic configurations.

Physically, the DM interaction arises as the leading order exchange interaction generated by spin-orbit interactions [64, 67]. In general, the spin-orbit interaction can give rise to additional anisotropic exchange interactions which are typically weaker than the DM interaction [64, 68]. In particular, for the pyrochlore lattice, there are two additional symmetry-allowed nearest-neighbor exchange couplings in the bilinear spin Hamiltonian [69, 70]. These two couplings correspond to a bond-dependent diagonal “Kitaev” interaction K [71], and a symmetric off-diagonal “pseudo-dipolar” interaction Γ [72]. When spin-orbit coupling is one of the dominant energy scales, these additional couplings cannot be ignored in general, as is the case in the rare-earth pyrochlore magnets [73]. The effect of a small but nonzero Γ/J is to induce a finite canting angle to the spins, leading to a non-colinear ferromagnetic configuration [65].

In this paper, we only consider the Heisenberg and DM interactions, while ignoring the remaining two symmetry-allowed couplings. Indeed, this model was shown to display colinear ferromagnetic order in both the classical and quantum scenarios [49], resulting in an accidental $O(3)$ degeneracy in the ground state manifold. From a material perspective, this model is justified in the regime where spin-orbit interactions can be treated perturbatively, in which case the isotropic Heisenberg coupling is expected to be the dominant exchange interaction, and the DM coupling is the leading order anisotropic exchange [49, 64]. This situation is relevant to $3d$ transition metal ions, where spin-orbit interactions are expected to be perturbatively small. This model is of particular relevance for the ferromagnetic materials $\text{Lu}_2\text{V}_2\text{O}_7$ and $\text{Y}_2\text{V}_2\text{O}_7$ which crystallize into a pyrochlore lattice, with a magnetic V^{4+} ion ($S = 1/2$) located at each lattice site [74–77]. Indeed, the realization of a colinear ferromagnet in $\text{Lu}_2\text{V}_2\text{O}_7$ is supported by thermal transport [78] and inelastic neutron scattering measurements [79], as well as density-functional theory calculations [68].

The remainder of this paper focuses on ObD in the ferromagnetic regime of Eq. (1) which, to the best of our knowledge, has not been explored previously. As discussed just above, the case of “weak DM” ($|D| < J$) is motivated by material realizations of this model in the context of transition metal pyrochlores. However, out of theoretical interest, we nevertheless extend our

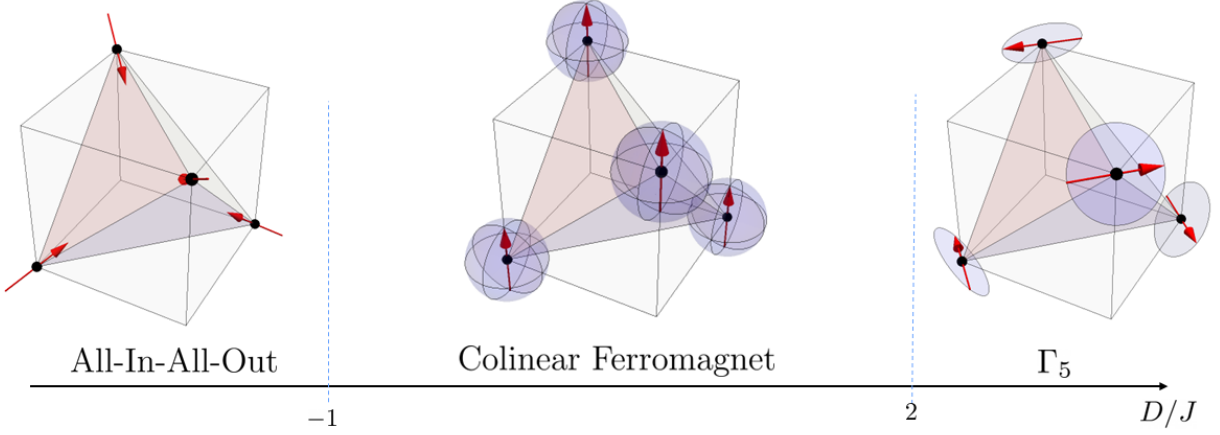


FIG. 1: Classical ground state configurations of the Hamiltonian in Eq. (1), depicted on a single tetrahedron of the pyrochlore lattice. The ground state configuration corresponds to colinear ferromagnet for $-1 < \frac{D}{J} < 2$, as well as the all-in-all-out and Γ_5 antiferromagnetic configurations for $\frac{D}{J} < -1$ and $\frac{D}{J} > 2$ respectively. The spheres and discs surrounding the spins illustrate manifolds of degenerate spin configurations.

analysis to the entirety of the ferromagnetic phase as depicted in Fig. 1. While we note that the region where $|D| > J$ may not have any particular relevance to real known materials at the present time, it is of theoretical interest in the broader context of a novel mechanism of ObD in the *absence* of quantum fluctuations. In the following section, we discuss the methods used to investigate ObD in the ferromagnetic regime of Eq. (1). Note that throughout this paper, calculations are carried out in units where $\hbar = k_B = 1$.

III. METHODS

In the present work, we make use of a number of methods to explore the selection mechanism of the global (bulk) magnetization per spin order parameter, denoted as \mathbf{m} , of Eq. (1). This section briefly discusses each of these methods and their implementation.

A. Classical low-temperature expansion

For the classical version of Eq. (1), the low-temperature selection of the magnetization direction as a function of the interaction parameter D/J can be analytically studied by producing a classical low-temperature expansion (CLTE) describing the thermal fluctuations about an ordered ground state configuration. The thermal selection of a specific ground state configuration is then obtained by considering a solvable quadratic effective theory in terms of the transverse fluctuations δn_i^α , where $\alpha = 1, 2$ labels the two transverse directions. At low temperatures, only small transverse displacements away from the local spin direction take place, i.e. $|\delta n_i^\alpha| \ll S$. Under this

assumption, the spins take the form

$$\mathbf{S}_i \simeq \delta n_i^1 \hat{\mathbf{e}}_1 + \delta n_i^2 \hat{\mathbf{e}}_2 + S \left(1 - \frac{(\delta n_i^1)^2}{2S^2} - \frac{(\delta n_i^2)^2}{2S^2} \right) \hat{\mathbf{m}}, \quad (2)$$

where $\hat{\mathbf{m}}$ is the magnetization polarization, and $\hat{\mathbf{e}}_1, \hat{\mathbf{e}}_2$ form an orthonormal triad with the ordering direction, i.e. $\hat{\mathbf{e}}_\alpha \cdot \hat{\mathbf{e}}_{\alpha'} = \delta_{\alpha\alpha'}$ and $\hat{\mathbf{m}} = \hat{\mathbf{e}}_1 \times \hat{\mathbf{e}}_2$. Substituting Eq. (2) into the Hamiltonian in Eq. (1) and keeping only the quadratic terms in δn_i^α results in an effective quadratic theory

$$\mathcal{H}_{\text{CLTE}}^{(\hat{\mathbf{m}})} = S^2 E_0 + \frac{1}{2} \sum_{\mathbf{q}} \sum_{\mu, \nu=0}^3 \sum_{\alpha, \beta=1}^2 \delta n_\mu^\alpha(-\mathbf{q}) H_{\alpha\beta, \mu\nu}^{(\hat{\mathbf{m}})}(\mathbf{q}) \delta n_\nu^\beta(\mathbf{q}), \quad (3)$$

where $S^2 E_0 = -12JNS^2$ is the classical ground state energy, N is the number of FCC unit cells, μ, ν label the sublattice structure, and

$$\begin{aligned} H_{\alpha\beta, \mu\nu}^{(\hat{\mathbf{m}})}(\mathbf{q}) \equiv & 6J\delta_{\alpha\beta}\delta_{\mu\nu} - 2J\delta_{\alpha\beta}(1 - \delta_{\mu\nu}) \cos(\mathbf{q} \cdot \mathbf{r}_{\mu\nu}) \\ & + 2D\mathbf{d}_{\mu\nu} \cdot \hat{\mathbf{m}}(-1)^\alpha (1 - \delta_{\alpha\beta})(1 - \delta_{\mu\nu}) \cos(\mathbf{q} \cdot \mathbf{r}_{\mu\nu}) \end{aligned} \quad (4)$$

is the Hessian matrix that results from the second derivatives of the classical energies of the fully polarized states with respect to the transverse spin fluctuations. The entropy associated with the fluctuations about a given polarized configuration $\hat{\mathbf{m}}$ is then given by the expression [65]

$$\mathcal{S}_{\hat{\mathbf{m}}} = \text{constant} - \frac{1}{2} \sum_{\mathbf{q}} \ln(\det H^{(\hat{\mathbf{m}})}(\mathbf{q})). \quad (5)$$

The thermal selection between the fully polarized states can be exposed by maximizing the entropy in Eq. (5) with respect to $\hat{\mathbf{m}}$.

B. Classical Monte Carlo

The finite temperature properties of the ferromagnetic phase of Eq. (1) are explored using classical Monte Carlo (MC) simulations. Simulations were carried out on a finite pyrochlore lattice with $4L^3$ spins with $L = 10$ and periodic boundaries, using both Metropolis importance sampling and over-relaxation updates [80–82], and averaged over 10 independent MC simulations. For each simulation, the system is initialized in a random configuration at high temperature $T > T_c$, and then gradually cooled down to the target temperature, thermalizing with 5×10^4 sweeps between each step in temperature. Each of the thermodynamic observables measured is averaged over 10^5 independent MC sweeps and then averaged over the independent simulations.

For the collinear ferromagnetic phase, the onset of long-range order is tracked by measuring the magnitude of the magnetization per spin

$$\mathbf{m} = \frac{1}{4N} \sum_i \mathbf{S}_i, \quad (6)$$

where $4N$ is the number of spins in a system consisting of N FCC unit cells. To investigate the evolution and selection of the orientation of the magnetization as a function of temperature, it is not enough to study the thermodynamic average of Eq. (6). Indeed, a generic Ginzburg-Landau (GL) expansion of the free energy for a system with cubic symmetry yields [83, 84]

$$\mathcal{F} = \frac{r}{2} |\mathbf{m}|^2 + \frac{u}{4} |\mathbf{m}|^4 + v (m_x^4 + m_y^4 + m_z^4) + \frac{w}{6} |\mathbf{m}|^6 + K (m_x^2 m_y^2 m_z^2) + \dots \quad (7)$$

where the coefficients $\{r, u, v, w, K\}$ are temperature dependent. The resulting terms can be broadly separated into isotropic terms, i.e. those involving powers of the magnitude of $|\mathbf{m}|$ in Eq. (7), which do not distinguish between different magnetization orientations and the anisotropic terms, which do. While the GL free energy in Eq. (7) is not necessarily valid away from the critical temperature, it motivates the lowest order symmetry allowed functions of the order parameter, which can distinguish between different orientations of the order parameter. In our MC simulations, we study the temperature evolution of the average magnetization per spin $\langle |\mathbf{m}| \rangle$, as well as the anisotropic observables

$$M_4 \equiv \langle m_x^4 + m_y^4 + m_z^4 \rangle, \quad (8)$$

$$\delta M_4 \equiv \frac{3}{2} (\langle |\mathbf{m}|^4 \rangle - M_4), \quad (9)$$

$$M_6 \equiv 27 \langle m_x^2 m_y^2 m_z^2 \rangle, \quad (10)$$

where $\langle \dots \rangle$ denotes thermal averaging, and the factors of 3/2 and 27 are added to normalize the values between 0 and 1. We refer to the anisotropic terms defined in Eqs. (8–10) as the *cubic parameters*. The values of the cubic parameters for magnetization along various high symmetry directions are listed in Table I. Note that throughout this work, we use the notation $\langle hkl \rangle$ to denote the real space vector $h\hat{x} + k\hat{y} + l\hat{z}$, along with all other symmetry-related directions.

To further investigate the evolution of the total magnetization vector, we sample the *instantaneous* magnetization direction of the system $\hat{\mathbf{m}} = \sum_i \mathbf{S}_i / |\sum_i \mathbf{S}_i|$ along each Cartesian direction 2×10^4 times for a set of temperatures ranging from $T \leq T_c$ to $T \ll T_c$. The resulting distribution, $p(\hat{\mathbf{m}})$, is visualized as a function of the polar and azimuthal angles, θ and ϕ , of the global magnetization restricted to the first octant where $\phi \in [0, \pi/2]$ and $\cos(\theta) \in [0, 1]$. Clustering of the total magnetization distribution about a given magnetization orientation is therefore considered to be evidence for a thermal selection of the corresponding magnetization direction.

C. Quantum spin waves

To investigate the putative thermal ObD selection in the low temperature quantum version of Eq. (1), we perform a Holstein-Primakoff spin wave expansion. In particular, spin operators are recast as Holstein-Primakoff bosons [85]

$$\begin{aligned} S_{\mathbf{R},\mu}^{(\hat{\mathbf{m}})} &= S - a_{\mathbf{R},\mu}^\dagger a_{\mathbf{R},\mu}, \\ S_{\mathbf{R},\mu}^+ &= (2S - a_{\mathbf{R},\mu}^\dagger a_{\mathbf{R},\mu})^{1/2} a_{\mathbf{R},\mu}, \\ S_{\mathbf{R},\mu}^- &= a_{\mathbf{R},\mu}^\dagger (2S - a_{\mathbf{R},\mu}^\dagger a_{\mathbf{R},\mu})^{1/2}, \end{aligned} \quad (11)$$

where $S_{\mathbf{R},\mu}^{(\hat{\mathbf{m}})} = \mathbf{S}_{\mathbf{R},\mu} \cdot \hat{\mathbf{m}}$ is the component of the spin operator aligned along the global polarization axis $\hat{\mathbf{m}}$ of the ferromagnetic configuration, and \mathbf{R} is an FCC lattice vector. In this picture, each boson is interpreted as a quantum of spin fluctuation about the ordered ground state. Plugging this transformation into the spin Hamiltonian in Eq. (1) and expanding the square root in powers of $a_{\mathbf{R},\mu}^\dagger a_{\mathbf{R},\mu} / 2S$ yields a semi-classical expansion

$$\mathcal{H} = \sum_{n=0}^{\infty} S^{2-n/2} \mathcal{H}_n^{(\hat{\mathbf{m}})}, \quad (12)$$

where each order of the expansion is now dependent on the global polarization axis. Truncating at $\mathcal{O}(S)$ gives the non-interacting magnon Hamiltonian

$$\mathcal{H}_{\text{QSW}}^{(\hat{\mathbf{m}})} = S^2 \mathcal{H}_0^{(\hat{\mathbf{m}})} + S^{3/2} \mathcal{H}_1^{(\hat{\mathbf{m}})} + S \mathcal{H}_2^{(\hat{\mathbf{m}})}. \quad (13)$$

Note that $\mathcal{H}_1^{(\hat{\mathbf{m}})} = 0$ whenever the spin configuration is classically metastable [17], in which case Eq. (13) simplifies

$$\begin{aligned} \mathcal{H}_{\text{QSW}}^{(\hat{\mathbf{m}})} &= S(S+1)E_0 + \\ &+ \frac{S}{2} \sum_{\mathbf{q}} \sum_{\mu,\nu=0}^3 [X_{\mu\nu}^{(\hat{\mathbf{m}})}(\mathbf{q}) a_{\mu,\mathbf{q}}^\dagger a_{\nu,\mathbf{q}} + X_{\nu\mu}^{(\hat{\mathbf{m}})}(-\mathbf{q}) a_{\mu,-\mathbf{q}}^\dagger a_{\nu,-\mathbf{q}}], \end{aligned} \quad (14)$$

where

$$X_{\mu\nu}^{(\hat{\mathbf{m}})}(\mathbf{q}) = 6J\delta_{\mu\nu} - 2(J - iD\mathbf{d}_{\mu\nu} \cdot \hat{\mathbf{m}})(1 - \delta_{\mu\nu}) \cos(\mathbf{q} \cdot \mathbf{r}_{\mu\nu}). \quad (15)$$

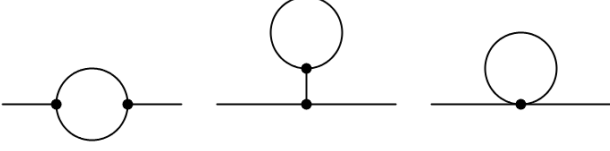


FIG. 2: Diagrams contributing to the magnon self-energy at $O(S^0)$ in the Holstein-Primakoff expansion. At $T = 0$, only the first diagram, connecting a pair of three-magnon interaction vertices, has a non-zero contribution. The explicit evaluation of these diagrams is discussed in Appendix C.

An appropriate unitary transformation of the magnon operators $a_{\mu,q} = \sum_{\alpha} U_{\mu,\alpha}^{(\hat{m})}(\mathbf{q}) b_{\alpha,q}$ brings Eq. (14) to the diagonal form

$$\mathcal{H}_{\text{QSW}}^{(\hat{m})} = S^2 E_0 + S E_2^{(\hat{m})} + S \sum_{\mathbf{q}} \sum_{\mu,\nu=0}^3 \omega_{\mu,\nu}^{(\hat{m})} b_{\mu,\mathbf{q}}^{\dagger} b_{\nu,\mathbf{q}}, \quad (16)$$

where $\omega_{\mu,\mathbf{q}}^{(\hat{m})}$ is the magnon dispersion and

$$E_2^{(\hat{m})} = E_0 + \frac{1}{2} \sum_{\mathbf{q}} \sum_{\mu=0}^3 \omega_{\mu,\mathbf{q}}^{(\hat{m})}, \quad (17)$$

is the $O(S)$ correction to the ground state energy from quantum zero-point fluctuations [17]. The free energy in linear spin-wave theory is then calculated as

$$\mathcal{F}^{(\hat{m})} = S^2 E_0 + S E_2^{(\hat{m})} + T \sum_{\mathbf{q}} \sum_{\mu=0}^3 \ln \left(1 - e^{-S \omega_{\mu,\mathbf{q}}^{(\hat{m})}/T} \right). \quad (18)$$

The selection of certain configurations over others is understood at this level by minimizing Eq. (18) with respect to the various classical ground state configurations. At $T = 0$, this amounts to minimizing the zero-point energy in Eq. (17), which is the typical approach taken to expose quantum ObD [38, 56, 62, 65]. At nonzero temperature, the last term in Eq. (18) must also be included, which may or may not select the same configurations as the zero-point contribution [48].

D. Nonlinear spin waves

To analyze the stability of the ferromagnetic phase, we extend our spin wave theory to include magnon-magnon interactions. Corrections to the linear spin-wave theory can be included perturbatively using the leading order magnon-magnon interactions in the $1/S$ expansion in Eq. (12), given by the symmetrized three-magnon and four-magnon interaction terms [86]

$$\mathcal{H}_3^{(\hat{m})} = \frac{1}{2! \sqrt{N}} \sum_{\mathbf{k}\mathbf{q}} \sum_{\mu\nu\lambda} \left[Y_{\mathbf{k},\mathbf{q}}^{\mu\nu\lambda}(\hat{\mathbf{m}}) a_{\mathbf{k},\mu}^{\dagger} a_{\mathbf{q},\nu}^{\dagger} a_{\mathbf{k}+\mathbf{q},\lambda} + \text{H.c.} \right] \quad (19)$$

and

$$\mathcal{H}_4^{(\hat{m})} = \frac{1}{N(2!)^2} \sum_{\mathbf{k}\mathbf{q}\mathbf{Q}} \sum_{\mu\nu\lambda\rho} V_{\mathbf{k},\mathbf{q},\mathbf{Q}}^{\mu\nu\lambda\rho}(\hat{\mathbf{m}}) a_{\mathbf{k}+\mathbf{Q},\mu}^{\dagger} a_{\mathbf{q}-\mathbf{Q},\nu}^{\dagger} a_{\mathbf{q},\lambda} a_{\mathbf{k},\rho}, \quad (20)$$

where the interaction vertices in $Y_{\mathbf{k},\mathbf{q}}^{\mu\nu\lambda}(\hat{\mathbf{m}})$ and $V_{\mathbf{k},\mathbf{q},\mathbf{Q}}^{\mu\nu\lambda\rho}(\hat{\mathbf{m}})$, are defined in Appendix C. To probe the stability of the ferromagnetic phase, we analyze the single-magnon spectrum at $T = 0$ in the presence of three and four-magnon interactions by numerically computing the magnon spectral function $\mathcal{A}(\mathbf{k}, \omega)$. This quantity is closely related to observables such as the dynamical structure factor [87], which is experimentally accessible using inelastic neutron scattering.

The single-magnon spectral function is given by [88]

$$\mathcal{A}(\mathbf{k}, \omega) = -\frac{1}{\pi} \text{Im} \left\{ \text{Tr} \left[\mathbf{G}_{\text{ret}}^{(\hat{m})}(\mathbf{k}, \omega) \right] \right\}, \quad (21)$$

where

$$\mathbf{G}_{\text{ret}}^{(\hat{m})}(\mathbf{k}, \omega) = \left[\omega - S \mathbf{\Omega}_{\mathbf{k}}^{(\hat{m})} - \mathbf{\Sigma}^{(\hat{m})}(\mathbf{k}, \omega) + i0^+ \right]^{-1}, \quad (22)$$

is the retarded magnon Green's function and $\left[\mathbf{\Omega}_{\mathbf{k}}^{(\hat{m})} \right]_{\mu\nu} = \delta_{\mu\nu} \omega_{\mu,\mathbf{k}}^{(\hat{m})}$ is the diagonalized linear-spin wave Hamiltonian. The (retarded) self-energy $\mathbf{\Sigma}^{(\hat{m})}(\mathbf{k}, \omega)$ arises from magnon-magnon interactions and can be included perturbatively in the $1/S$ expansion. At $O(S^0)$, the self-energy is calculated by evaluating the one-loop Feynman diagrams depicted in Fig. 2, where at $T = 0$ we find that only the leftmost diagram has a non-zero contribution (see Appendix C for more details). In this case, the components of the self-energy matrix are evaluated as

$$\Sigma_{\mu\nu}^{(\hat{m})}(\mathbf{k}, \omega) = \frac{S}{2N} \sum_{\mathbf{q}} \sum_{\alpha\beta} \frac{\left(T_{\mathbf{q},\mathbf{k}-\mathbf{q}}^{\alpha\beta\mu}(\hat{\mathbf{m}}) \right) \left(T_{\mathbf{q},\mathbf{k}-\mathbf{q}}^{\alpha\beta\nu}(\hat{\mathbf{m}}) \right)^*}{\omega + i0^+ - S \omega_{\alpha,\mathbf{k}-\mathbf{q}}^{(\hat{m})} - S \omega_{\beta,\mathbf{q}}^{(\hat{m})}}, \quad (23)$$

where the $T_{\mathbf{k},\mathbf{q}}^{\mu\nu\lambda}(\hat{\mathbf{m}})$ coefficients are the three-magnon vertices in the basis which diagonalizes the linear spin wave theory. A more detailed derivation of Eq. (23) can be found in Appendix C.

In the absence of magnon-magnon interactions, the single-magnon excitations have an infinite lifetime and appear as sharp delta function peaks. In general, the self-energy will consist of both real and imaginary parts, which will renormalize and broaden the single-magnon spectrum respectively, the latter of which is interpreted as the magnons acquiring a finite quasiparticle lifetime. In practice, the self-energy components are calculated by numerically computing the sum over wavevectors in Eq. (23) with a finite broadening factor $0^+ \approx 10^{-4}$, and is then used to calculate the $1/S$ correction to the bare Green's function using Eq. (22).

IV. RESULTS

In this section, we present results regarding ObD the ferromagnetic regime of Eq. (1), for both the classical and quantum models. We begin our discussion of ObD with a purely classical outlook on the entropic selection of the magnetization order parameter, using the classical low-temperature expansion (CLTE) supplemented with classical Monte Carlo (MC) simulations. Next, we study the ObD selection in the quantum case by using linear spin-wave theory. Finally, we extend this to non-linear spin-wave theory to analyze the stability of the ferromagnetic ground state in the purely quantum model.

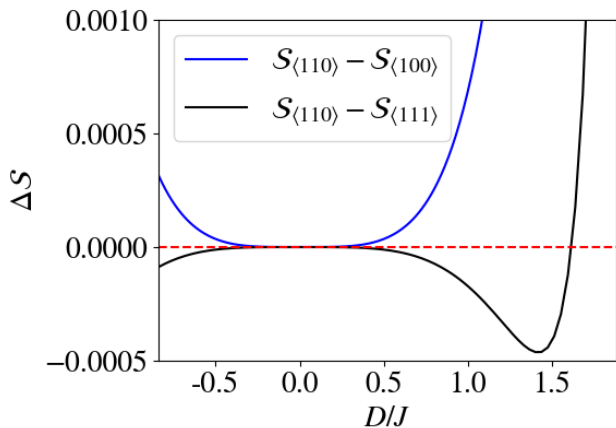


FIG. 3: Thermodynamic entropy from the CLTE about a ferromagnetic ground state. The entropy difference between the $\langle 110 \rangle$ and the $\langle 100 \rangle$ (blue line), and the $\langle 110 \rangle$ and the $\langle 111 \rangle$ (black line) cubic directions is calculated using Eq. (5). We note that the entropy is maximized for magnetization along the $\langle 111 \rangle$ direction for $-1 < D/J \lesssim 1.66$ and along the $\langle 110 \rangle$ direction for $1.66 \lesssim D/J < 2$, except at $D/J = 0$ when the magnetization is isotropic.

A. Classical selection

As a first approach to expose the ObD thermal selection, we use the CLTE to study the preferred orientation of the net magnetization at low temperature ($0 < T \ll T_c$). We note that in the classical low-temperature limit, the equipartition theorem guarantees that the free energy is minimized by the maximal entropy configurations

We calculate the entropy using Eq. (5) for magnetization along the $\langle 100 \rangle$, $\langle 110 \rangle$, and $\langle 111 \rangle$ cubic directions, as shown in Fig. 3. This calculation identifies two distinct regimes, one for $D/J \in (-1, 1.66)$ and another for $D/J \in (1.66, 2)$, where a magnetization along the $\langle 111 \rangle$ and $\langle 110 \rangle$ directions respectively maximize the entropy. We also note that the entropy difference grows as the ratio D/J approaches the phase boundaries with the AFM ordered phases, see Fig. 1.

Although the CLTE calculation of the entropy already predicts a selection of the magnetization at low temperatures, we cannot assume that the same state selection remains as the temperature increases upon approaching T_c . Indeed, taking the example of Γ_5 phase depicted in Fig. 1, it was previously found that different states may be selected near the critical temperature $T \lesssim T_c$, compared to the low-temperature selection at $T \ll T_c$ [49]. We use classical MC simulations to track the evolution of the magnetization direction [49, 55]. We record the magnetization direction, $\hat{\mathbf{m}} = \sum_i \mathbf{S}_i / |\sum_i \mathbf{S}_i|$, to produce a distribution $p(\hat{\mathbf{m}})$ as a function of temperature. This distribution function then provides a direct probe of the free energy difference between configurations, given by

$$\frac{p(\hat{\mathbf{m}})}{p(\hat{\mathbf{n}})} = \exp\left(-\frac{\mathcal{F}(\hat{\mathbf{m}}) - \mathcal{F}(\hat{\mathbf{n}})}{T}\right). \quad (24)$$

In other words, the configuration minimizing the free energy

occurs when $p(\hat{\mathbf{m}})$ is maximized. We therefore refer to a magnetization direction as being “selected” if it is the most probable orientation to occur at the specified temperature. For clarity, and without loss of generality, we present the distribution $p(\hat{\mathbf{m}})$ solely in the first octant of the Cartesian coordinates system and use the spherical parametrization for the total magnetization where θ and ϕ are the polar and azimuthal angles, respectively.

To illustrate the evolution of the thermal selection via the evolution of the total magnetization distribution, we present the temperature evolution of the distribution $p(\hat{\mathbf{m}})$ as a function of temperature in Fig. 4 for two values of the DM interaction: one with $D/J \simeq 1.43$ and another with $D/J \simeq 1.73$. As will be made clear later, these two values of D/J have been chosen as they each illustrate distinct temperature-dependant magnetization distribution functions. Figures 4 (a)-(d) illustrate the evolution of the total magnetization distribution as a function of temperature for the system with the ratio $D/J \simeq 1.43$. At temperatures above the critical temperature, $T > T_c$, the total magnetization distribution shown in Fig. 4(a) uniformly $O(3)$ distributed, a consequence of the absence of long-range magnetic order. Just below the critical temperature, $T \lesssim T_c$, our MC simulations reveal that the distribution $p(\hat{\mathbf{m}})$ shown in Fig. 4(b) clusters around the points $\cos(\theta) \in \{0, 1\}$ and $\phi \in \{0, \pi/2\}$. These clusters indicate that the magnetization aligns with the $\langle 100 \rangle$ directions near the critical temperature. As temperature is decreased, a triangle-shaped pattern develops, where the distribution clusters around $\phi = \pi/4$ and $\cos(\theta) = 1/\sqrt{3}$ (see Fig. 4(c) and (d)). The center of the triangle corresponds to an orientation of the total magnetization along the $\langle 111 \rangle$. We note that the variance of the distribution becomes smaller as the temperature is lowered, implying that the selection of the $\langle 111 \rangle$ orientation becomes stronger at lower temperatures.

Figures 4 (c)-(h) illustrate the evolution of the total magnetization distribution as a function of temperature for the system with a $D/J \simeq 1.73$ value. We note that for this set of parameters, the system develops three distinct patterns in the distribution of the magnetization direction as a function of temperature. For $T \lesssim T_c$, the magnetization is similarly oriented along one of the $\langle 100 \rangle$ directions, as shown in Fig. 4(f). As the temperature is further decreased, the triangular pattern develops, indicating a preference to order along the $\langle 111 \rangle$ directions (Fig. 4(g)), analogous to Figs. 4(a-c). In contrast however, as the system is cooled down into the low-temperature region, the magnetization distribution shows clustering at three distinct lobes, centered around the points $(\cos(\theta), \phi) \in \{(1/\sqrt{2}, 0), (0, \pi/4), (1/\sqrt{2}, \pi/2)\}$. These magnetization directions correspond to the $\langle 110 \rangle$ directions. As the temperature is further decreased, there are no more qualitative changes in the pattern of the distribution.

Altogether, the evolution of the magnetization distributions $p(\hat{\mathbf{m}})$ shown in Fig. 4 for the two representative values of D/J suggests that the collinear ferromagnetic phase of the Hamiltonian (1) presents *at least* two distinct ordered phases for a given set of interaction parameters. The range in temperature and ratio D/J where these phases are observed, however, is not easily identified through the sole measurement of the distribution $p(\hat{\mathbf{m}})$. To provide an approximate identification of the boundaries between the different magnetization orien-

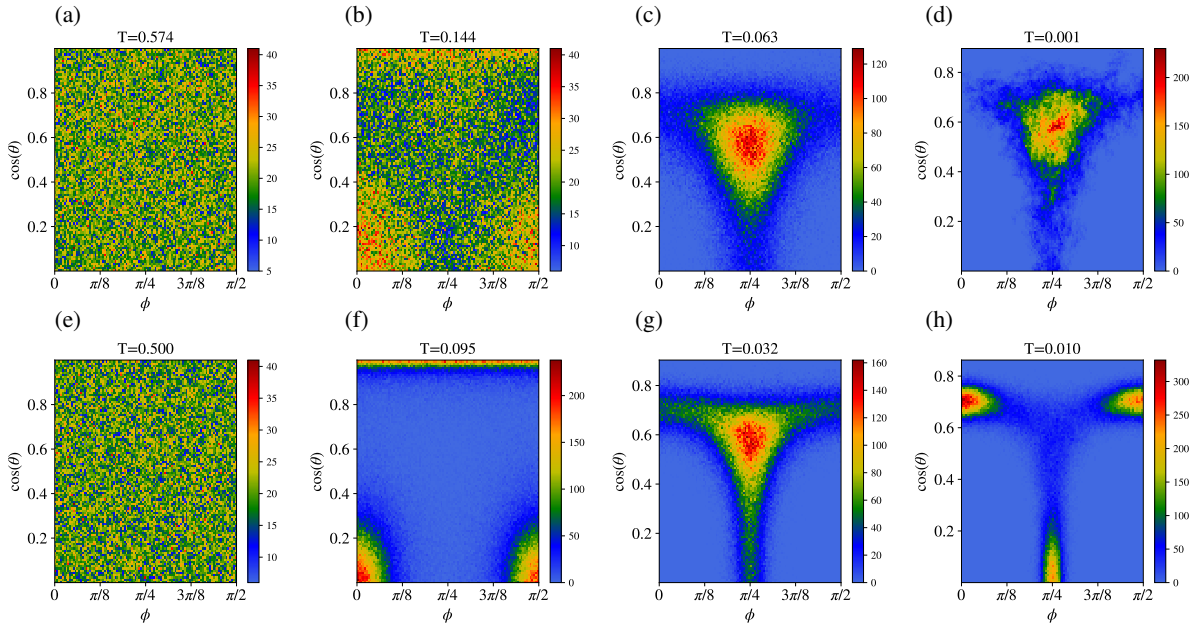


FIG. 4: Distribution of the global magnetization direction from classical Monte Carlo simulations for the two systems labeled by the white dot-dashed lines in Fig.5(d). Sub-figures (a-d) correspond to the left-most white line in Fig.5(d), that is to $D/J = 1.42$, while sub-figures (e-h) correspond to the right-most white line in Fig.5(d) where $D/J = 1.73$, shown for decreasing temperatures when read left to right.

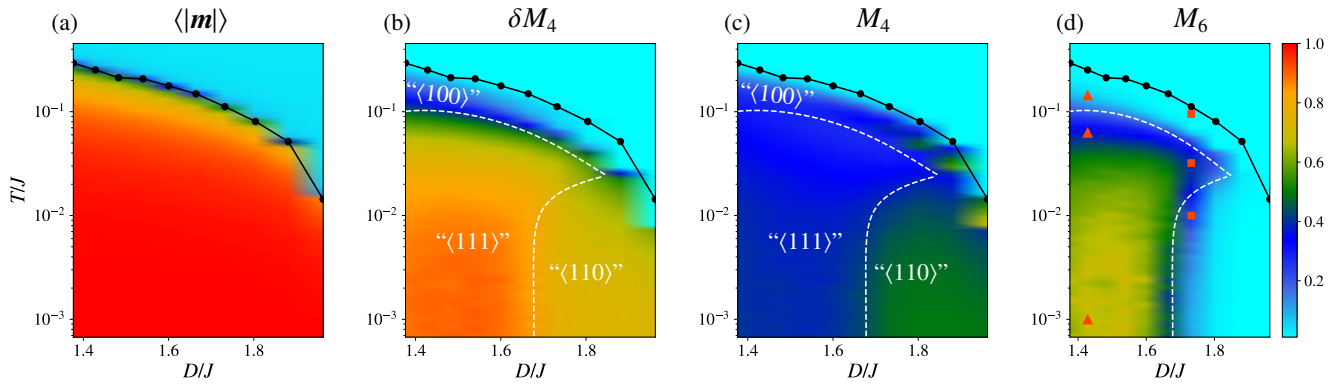


FIG. 5: Thermal evolution of the (a) magnetization per spin $\langle |m| \rangle$, and the anisotropic cubic parameters (b) δM_4 , (c) M_4 , and (d) M_6 as defined in Eqs. (8-10). Sub-figures (b) and (c) illustrate the three regions where a distinct easy axis for the magnetization is chosen from ObD. The triangles in sub-figure (d) label the temperatures at which the magnetization distribution was measured as illustrated in Fig. 4(b-d), and the squares correspond to Fig. 4(f-h). The white dashed lines in sub-figures (b)-(d) are guides to the eye, and the directions are indicated in quotation marks to emphasize the fact that these regions are chosen qualitatively based on the distinct values of the cubic parameters.

tations, we study the temperature evolution of the thermally averaged cubic parameters δM_4 , M_4 and M_6 (as defined in Eqs. (8-10)), to provide a coarse phase diagram as a function of temperature and D/J , shown in Fig. 5(a-d). The critical temperature T_c is marked by the black dots, determined by the onset of a nonzero magnetization $\langle |m| \rangle$ in Fig. 5(a). We note that the critical temperature collapses to zero in the limit $D/J \rightarrow 2^-$, corresponding to the spin-liquid phase discussed in Ref. [89]. The white dashed lines on Fig. 5(b-d) are drawn as guides to the eye to separate regions of distinct values of the cubic parameters. In Fig. 5(d), the locations at which the

magnetization distributions $p(\hat{m})$ were calculated are marked with triangles corresponding to Fig. 4(b-d) and squares corresponding to Fig. 4(f-h). By comparing the regions separated by the white lines with the distributions in Fig. 4, we are able to qualitatively identify that these regions coincide with magnetization along distinct directions. These ordering directions are labelled in Fig. 5(b,c) in quotation marks, to make clear that these regions are approximate. We observe that the (extrapolated) zero-temperature boundary separating the $\langle 111 \rangle$ and $\langle 110 \rangle$ regions is around $D/J \sim 1.66$, which is consistent with CLTE entropy calculation shown in Fig. 3. Further details

regarding the calculation of the cubic parameters can be found in Appendix B.

B. Quantum selection at $T \ll T_c$

Within the classical ferromagnetic regime, the ground state manifold has full rotational symmetry, however this degeneracy is accidental whenever the DM interaction is present. In a typical scenario, one might expect that quantizing the Hamiltonian in Eq. (1) would partially lift the accidental degeneracy between classical ground states due to the zero-point fluctuations in Eq. (17). In the present case, we consider a fully polarized product state oriented along a global magnetization unit vector \hat{m} :

$$|\hat{m}\rangle \equiv \bigotimes_{i=1}^{4N} |\uparrow_{\hat{m}}\rangle_i, \quad (25)$$

where $|\uparrow_{\hat{m}}\rangle_i$ is the eigenstate of the spin operator $S_i \cdot \hat{m}$ corresponding to the maximum eigenvalue. We find that

$$\begin{aligned} \mathcal{H}|\hat{m}\rangle &= S^2 E_0 |\hat{m}\rangle + iDS \sum_{\langle i,j \rangle} \mathbf{d}_{ij} \cdot (\hat{\mathbf{e}}_1 + i\hat{\mathbf{e}}_2) S_i^- |\hat{m}\rangle \\ &= S^2 E_0 |\hat{m}\rangle, \end{aligned} \quad (26)$$

where it is straightforward to verify that the sum over nearest-neighbor DM vectors vanishes from Eq. (A2). That is to say, $|\hat{m}\rangle$ is an *exact* eigenstate of the quantum many-body Hamiltonian in Eq. (1). Any fully polarized configuration therefore has no zero-point fluctuations, and the accidental degeneracy persists in the fully quantum model. This peculiar scenario motivates our investigation of (thermal) ObD in the ferromagnetic phase of this model.

Since the fully polarized product state is an exact eigenstate of the Hamiltonian, we combine Eq. (26) with Eq. (16) to find that $E_2^{(\hat{m})} = 0$. More generally, the classical ground state energy is equivalent to the energy of the ferromagnetic product state in the quantum model, implying that there are no quantum zero point fluctuations in the ferromagnetic phase. At finite temperature, the ObD selection can be exposed by minimizing the free energy difference

$$\mathcal{F}^{(\hat{m})} - \mathcal{F}^{(\hat{n})} = T \sum_q \sum_{\mu=0}^3 \ln \left(\frac{1 - e^{-S\omega_{\mu,q}^{(\hat{m})}/T}}{1 - e^{-S\omega_{\mu,q}^{(\hat{n})}/T}} \right) \quad (27)$$

with respect to \hat{m} , relative to a fixed reference magnetization axis \hat{n} .

Comparing the free energy difference between configurations using Eq. (27), we find that there are two distinct scenarios as depicted in Fig. 6, where the magnetization is directed along either the $\langle 111 \rangle$ or $\langle 110 \rangle$ directions. In contrast with the Monte Carlo simulations, where a selection of the $\langle 100 \rangle$ directions was found for $T \lesssim T_c$ (c.f. Fig. 5(b-d)), linear spin-wave theory does not capture this selection.

By calculating which configurations minimize the free energy in Eq. (27), we construct a low-temperature phase diagram depicted in Fig. 7 for the case where $S = 1/2$. We find that the

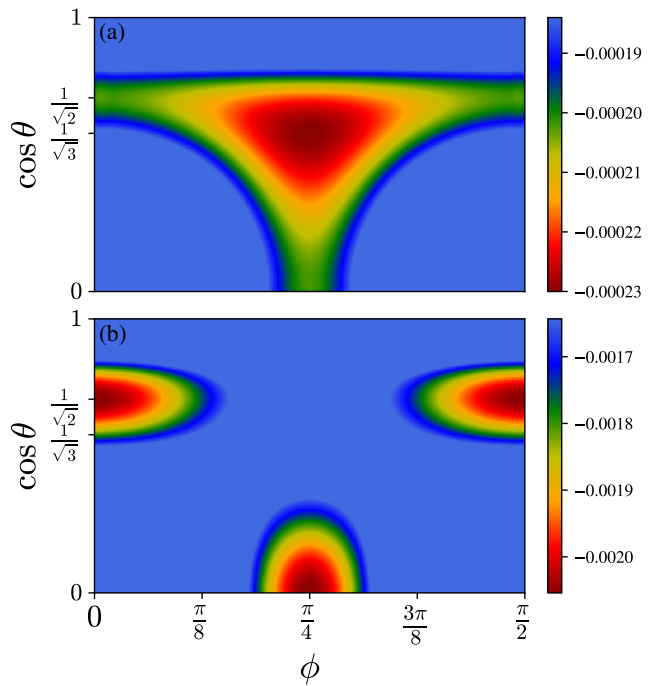


FIG. 6: Free energy difference between configurations obtained from linear spin-wave theory using Eq. (27) with $T/J = 0.1$, $\hat{n} = \langle 100 \rangle$ and $S = 1/2$. Panel (a) depicts the free energy distribution for $D/J = 1.0$, which is minimized by $\hat{m} = \langle 111 \rangle$. Panel (b) depicts the free energy distribution for $D/J = 1.8$, which is minimized by $\hat{m} = \langle 110 \rangle$.

$\langle 110 \rangle$ direction is selected for a region of the phase diagram in the range $1.2 \lesssim D/J < 2$, while the $\langle 111 \rangle$ direction is selected otherwise. The white region could not be resolved numerically, the free energy difference between configurations being smaller than $10^{-7}J$. This is expected, as the ObD selection vanishes both when $D \rightarrow 0$ (approaching the Heisenberg limit) or $T \rightarrow 0$. Note that the phase diagram depicts a region of re-entrance for a large indirect DM interaction, an intermediate region where a $\langle 110 \rangle$ selection is observed between both a high and low temperature $\langle 111 \rangle$ selection.

Although the fully polarized product state is an exact eigenstate as shown in Eq. (26), it is not necessarily the case that this eigenstate is the true many-body ground state outside of the perturbative regime $|D| \ll J$. Recent work investigating the quantum ground states of this model using functional renormalization group methods identified a ferromagnetic ordered state for $-1 < D/J \lesssim 1.3$, as well as a lack of conventional magnetic order for $1.3 \lesssim D/J \leq 2$ [49]. Indeed, this suggests that Eq. (25) is the ground state when $-1 < D/J \lesssim 1.2$, while for $1.2 \lesssim D/J \leq 2$ there is an entangled eigenstate which is lower in energy. To build on these findings, we show that the breakdown of long-range ferromagnetic order can be captured to lowest order in non-linear spin wave theory.

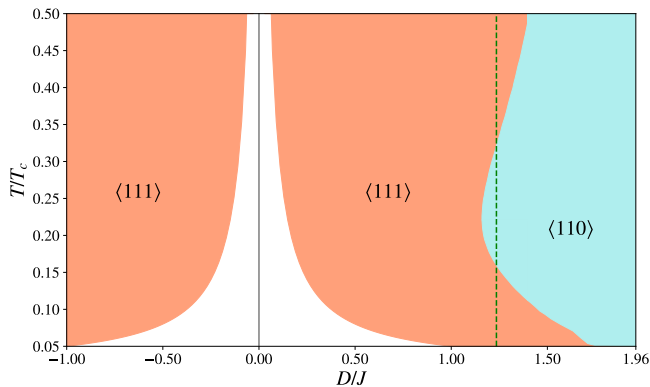


FIG. 7: Low temperature phase diagram obtained from linear spin-wave theory using Eq. (27) and $S = 1/2$. The black line at $D/J = 0$ is the Heisenberg line, where the model has an exact $O(3)$ symmetry and no ObD selection. The free energy difference could not be resolved numerically in the white region surrounding the Heisenberg line. The dashed line corresponds to the non-linear spin-wave instability as described in Sec. IV C. The temperature axis is scaled by the critical temperature T_c obtained from classical Monte Carlo simulations.

C. Limit of Stability

While Eq. (26) shows that the ferromagnetic product state is an exact eigenstate, it is not necessarily the true quantum ground state of Eq. (1) for all $-1 < D/J < 2$. To address the question of stability of the ferromagnetic ordered phase, we use non-linear spin-wave theory to calculate the $O(S^0)$ correction to the single-magnon spectral function at $T = 0$, using Eq. (21). Analogous to linear spin-wave theory, where a classical instability is characterized by the appearance of soft modes, we investigate whether there are soft modes in the renormalized spectrum for all $-1 < D/J < 2$.

Given that the ferromagnetic configuration is characterized by an accidental $O(3)$ degeneracy, persisting in the quantum model, at least one gapless mode is guaranteed to be observed in the linear spin-wave theory at $\mathbf{q} = \mathbf{0}$ — the pseudo-Goldstone mode [90, 91]. In the presence of quantum fluctuations, the pseudo-Goldstone mode generically becomes gapped at $O(S^0)$ in the self-energy [92]. However, the fact that the ferromagnetic configuration is an exact eigenstate of the Hamiltonian implies that this mode remains gapless at all orders of the $1/S$ expansion at $T = 0$, a somewhat peculiar property of the current model. Conversely, the accidental degeneracy is lifted by thermal fluctuations, leading to the dynamical generation of a pseudo-Goldstone gap at nonzero temperature [93]. Since our self-energy calculations are strictly carried out at $T = 0$, the pseudo-Goldstone mode remains gapless. We therefore look for instabilities in the form of additional soft modes in the magnon spectral function.

The results of these calculations are depicted in Fig. 8, showing the single-magnon spectral function to $O(S^0)$ in non-linear spin-wave theory. As D/J becomes large, the optical magnon bands become significantly broadened displaying a Lorentzian-

like form in frequency space. This broadening originates from decay effects, the width of the Lorentzian profile close to the spectral peaks is precisely the decay rate, encoded in the imaginary part of the self-energy. The three-body interaction couples the single-magnon excitations with the two-magnon continuum, and the non-analytic behavior observed in the spectral function generically corresponds to regions where the single magnon branch intersects with the boundary of the two-magnon continuum [94]. Additionally, the self-energy renormalizes the spectral function peaks, however, we find that there is a stable and gapless pseudo-Goldstone mode at $\mathbf{q} = \mathbf{0}$ for all $-1 < D/J < 2$ as expected.

We find that the second magnon branch becomes soft and shifts to negative frequencies at $\mathbf{q} = \mathbf{0}$ for a large and indirect DM interaction, as depicted in Fig. 8(b-c). In particular, the second branch becomes soft at a critical DM interaction $D/J \approx 1.235$, indicating that the long-range ferromagnetic order becomes unstable at $O(S^0)$ in the non-linear spin-wave theory for $1.235 \lesssim D/J < 2$. The location of the instability was calculated for $\hat{\mathbf{m}} = \langle 100 \rangle, \langle 110 \rangle, \langle 111 \rangle$ and is found to be independent of the classical magnetization direction $\hat{\mathbf{m}}$. For reference, the instability is marked by the dashed line on the linear spin-wave phase diagram in Fig. 7, and we note that the instability approximately coincides with the value of the DM interaction where $\langle 110 \rangle$ order is found. The region of instability $1.2 \lesssim D/J < 2$ is consistent with a pseudo-fermion functional renormalization group calculation for the same model in Ref. [49], where the authors did not detect any long-range magnetic order for $1.3 \lesssim D/J < 2$. Conversely, Noculak *et al.* report conventional magnetic order for all $D/J > 2$, corresponding to the Γ_5 phase in Fig. 1 [49]. One may speculate that the proximity of this instability in the phase diagram of Fig. 1 could be a result of the antiferromagnetic Γ_5 order “invading” into the classically ferromagnetic region. However, the phase diagram in Ref. [49] suggests that this is not the case. Our results rather suggest that the ferromagnetic product state in Eq. (25) is the exact ground state of Eq. (1) for $-1 \lesssim D/J \lesssim 1.2$, and that the phase diagram in Fig. (7) is accurate in this region. In particular, the existence of ObD in the absence of quantum zero-point fluctuations is a novel feature of this model.

V. DISCUSSION AND CONCLUSION

In this work, we studied the classical and quantum order-by-disorder selection of a collinear ferromagnetic phase of the Heisenberg and Dzyaloshinskii-Moriya Hamiltonian on the pyrochlore lattice. In the classical model, we found three distinct regions in parameter space *and* as a function of temperature where three distinct magnetization orientations are thermally selected. For large and indirect DM interaction $D \lesssim 2$, a cascade of re-orientations of the magnetization direction is observed as a function of temperature as depicted in Fig. 4(b). Motivated by our classical MC results for $T \lesssim T_c$, the behavior of the observed ferromagnetic transition is consistent with that of an $O(3)$ vector model with cubic anisotropy, governed by the Ginzburg-Landau-Wilson (GLW) free-energy functional

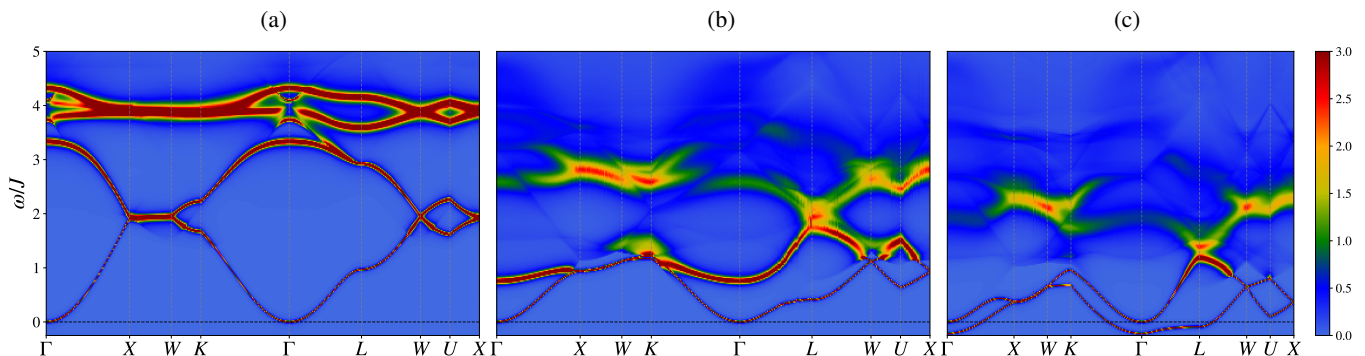


FIG. 8: Zero-temperature magnon spectral function $\mathcal{A}(\mathbf{k}, \omega)$ for $\hat{\mathbf{m}} = \langle 111 \rangle$ and $S = 1/2$ to $\mathcal{O}(S^0)$ in non-linear spin-wave theory, calculated using Eq. (21) for (a) $D/J = 0.25$, (b) $D/J = 1.00$ and (c) $D/J = 1.3$.

[95]

$$\mathcal{F}[m] \approx \int d^3x \left[\frac{1}{2} \sum_{\mu=1}^3 (\nabla m_{\mu})^2 + \frac{r}{2} |m|^2 + \frac{u}{4} |m|^4 + v \sum_{\mu=1}^3 m_{\mu}^4 \right]. \quad (28)$$

When $v > 0$, the cubic anisotropy favors the magnetization to be aligned with the $\langle 111 \rangle$ directions, while $v < 0$ favors the magnetization to be aligned with the $\langle 001 \rangle$ directions. From a renormalization group perspective, the $O(n)$ vector model with cubic anisotropy in three dimensions has a critical order parameter dimension $n = n_c$, below which the Heisenberg fixed point is stable and above which the cubic fixed point is stable [84]. Incidentally, $n_c \approx 3$ [96, 97], and it remains an open problem as to which of the fixed points of Eq. (28) are stable, so we are unable to comment on the universality class of this ferromagnetic transition. In contrast, Eq. (28) does not predict a $\langle 110 \rangle$ orientation which is observed in our classical MC simulations in the region where $D/J \rightarrow 2$. This would require, for example, the addition of a 6th order term to the GLW free energy, similar to the terms appearing in Eq. (7). In this same region, our MC simulations suggest that the phase transition becomes first-order. Additionally, the critical temperature completely vanishes at the boundary between the collinear ferromagnet and the Γ_5 phase ($D/J = 2$), where a novel spin liquid has been recently observed, characterized by fluctuating rank-1 vector and rank-2 tensor gauge fields [89]. Investigating the relationship between the failure of the GLW theory, the proximity to the novel spin liquid phase, and the observation of the $\langle 110 \rangle$ phase are left for future work.

In the quantum model, we find that the fully polarized product state in Eq. (25) is an exact eigenstate of the Hamiltonian regardless of the magnetization direction, and therefore the accidental degeneracy of the ferromagnetic phase is not lifted by zero-point fluctuations at $T = 0$. This accidental degeneracy is however lifted by the low-energy spin-wave excitations at nonzero temperature ($T > 0$), leading to a selection of a discrete set of magnetization directions as depicted in Fig. 7. This is the first realization of such an ObD mechanism that we are aware of where the selection of an ordered phase in a quantum system is purely thermal.

Using non-linear spin wave theory, we found that the ferromagnetic order does not persist for $D/J \gtrsim 1.235$. Coincidentally, this coincides reasonably well with the region in both our

MC simulations and linear spin-wave calculations which separates regions where different orientations of the magnetization are found (see Fig. 4 and Fig. 7). The nonlinear spin-wave instability in the region $1.235 \lesssim D/J < 2$ suggests the possibility of realizing a quantum paramagnetic or spin-liquid phase, and warrants further investigation.

We expect that the results obtained in the present work have implications in real ferromagnetic materials where the DM interaction is the leading perturbation. In particular, the magnetism of the ferromagnetic Mott insulators $\text{Lu}_2\text{V}_2\text{O}_7$ and $\text{Y}_2\text{V}_2\text{O}_7$ is rather well described by Eq. (1) [76, 77, 79]. Measurements of the magnetization of $\text{Lu}_2\text{V}_2\text{O}_7$ in Ref. [78] appear to be anisotropic with respect to the applied field direction, which could be related to ObD in this material. Recently, it was proposed in Ref. [93] that the thermal contribution to ObD can be diagnosed by a temperature-dependent energy gap measured via inelastic neutron scattering. We expect this would be the strongest experimental signature of ObD in these materials.

We also note that a much more general class of spin models are expected to exhibit ObD without zero-point fluctuations. Any ferromagnetic Heisenberg model with DM interactions will satisfy Eq. (26), as long as the sum over DM vectors along the bonds surrounding each site vanishes. We then expect that the ferromagnetic product state will remain the exact ground state of such a Hamiltonian as long as the DM interactions are sufficiently small with respect to the Heisenberg exchange J . Our calculations may then serve as a template to study ObD in these models.

ACKNOWLEDGMENTS

The authors acknowledge useful discussions with Subhankar Khatua, Johannes Reuther, Yasir Iqbal, Rajiv Singh, Jeffrey Rau, Itamar Aharony and Kristian Chung. We thank Vincent Noculak for comments on an early version of the manuscript. AH acknowledges support from the NSERC of Canada CGS-D Scholarship. DLG acknowledges financial support from the DFG through the Hallwachs-Röntgen Postdoc Program of the Würzburg-Dresden Cluster of Excellence on Complexity and Topology in Quantum Matter – *ct.qmat* (EXC 2147, project-id 390858490) and through SFB 1143 (project-id 247310070). The work at the University of Waterloo was supported by

the NSERC of Canada and the Canada Research Chair (Tier 1, M.J.P.G.) program. This research was enabled in part by computing resources provided by the Digital Research Alliance of Canada.

Appendix A: Pyrochlore lattice convention

The pyrochlore lattice is a face-centered cubic (FCC) lattice with four sites per unit cell. The primitive FCC lattice vectors are given by

$$\mathbf{a}_1 = \frac{a}{2}(\hat{\mathbf{y}} + \hat{\mathbf{z}}) \quad \mathbf{a}_2 = \frac{a}{2}(\hat{\mathbf{x}} + \hat{\mathbf{z}}) \quad \mathbf{a}_3 = \frac{a}{2}(\hat{\mathbf{x}} + \hat{\mathbf{y}}). \quad (\text{A1})$$

At each FCC lattice site, there is a spin of type 0. The remaining three spins within a unit cell are separated by the sublattice vectors $\mathbf{r}_{0\mu} = \mathbf{a}_\mu/2$. The sublattice vectors between a spin of type μ to a spin of type ν can then be constructed as $\mathbf{r}_{\mu\nu} \equiv \mathbf{r}_{0\nu} - \mathbf{r}_{0\mu}$.

The (indirect) DM vectors in this representation are given by

$$\begin{aligned} \mathbf{d}_{01} &= \hat{\mathbf{y}} - \hat{\mathbf{z}} & \mathbf{d}_{02} &= \hat{\mathbf{z}} - \hat{\mathbf{x}} & \mathbf{d}_{03} &= \hat{\mathbf{x}} - \hat{\mathbf{y}} \\ \mathbf{d}_{12} &= \hat{\mathbf{x}} + \hat{\mathbf{y}} & \mathbf{d}_{31} &= \hat{\mathbf{x}} + \hat{\mathbf{z}} & \mathbf{d}_{23} &= \hat{\mathbf{y}} + \hat{\mathbf{z}}, \end{aligned} \quad (\text{A2})$$

where the remaining DM vectors can be determined using the antisymmetry property $\mathbf{d}_{ji} = -\mathbf{d}_{ij}$. Note that in this representation, the DM vectors are unnormalized, with $|\mathbf{d}_{ij}| = \sqrt{2}$ when $i \neq j$.

Appendix B: Monte Carlo calculation of M_4 , δM_4 and M_6

The values of the cubic parameters M_4 , δM_4 and M_6 in Eqs. (8-10) were calculated using classical Monte Carlo to identify anisotropy in the magnetization direction as depicted in Fig. 5. If the magnetization is isotropic, the values of the cubic parameters will be distinct from the case where an easy axis is present, as shown in Table I.

	M_4	δM_4	M_6
Isotropic	3/5	3/4	9/35
$\langle 100 \rangle$	1	0	0
$\langle 110 \rangle$	1/2	3/4	0
$\langle 111 \rangle$	1/3	1	1

TABLE I: Expected values of the cubic parameters in Eqs. (8-10) for magnetization along different directions.

In Fig. 5(d), we mark with triangles (squares) the locations at which the distributions $p(\hat{\mathbf{m}})$ shown in Fig. 4(b-d) [Fig. 4(f-h)] were measured below the critical temperature. The temperature evolution of the cubic parameters identifies three distinct regions in both temperature T and DM interaction D/J shown in Fig. 5(b-d) where the white dashed lines are guides to the eye separating identified phases. The first temperature region, which we label “ $\langle 100 \rangle$ ”, is observed just below the critical

temperature T_c for $1 \lesssim D/J < 2$. In this region, all cubic parameters measured deviate from the isotropic values, see Fig. 5(b)-(d). In particular, we note that both the δM_4 and the M_6 cubic parameters acquire small values well below the isotropic limit, which are consistent with a $\langle 100 \rangle$ magnetization orientation. As expected, the deviation of the cubic parameters from the isotropic values increases as D/J increases. The second region, which we label region “ $\langle 111 \rangle$ ”, is delimited at low temperatures by the interaction ranges $-1 < D/J \lesssim -0.1$ and $0.1 < D/J \lesssim 1.3$. In the “ $\langle 111 \rangle$ ” region, the cubic parameters δM_4 , M_4 , and M_6 evolve smoothly, plateauing to the approximate values 9/10, 1/3, and 7/10, respectively, see Fig. 5(b-d). We note that the cubic parameters in this region suggest a $\langle 111 \rangle$ selection where all of the cubic parameters are non-vanishing. The third region, which we label region “ $\langle 110 \rangle$ ”, is delimited at low temperatures to the interaction parameters $1.3 \lesssim D/J < 2$, and delimited at higher temperatures by regions “ $\langle 100 \rangle$ ” and “ $\langle 111 \rangle$ ”. In the “ $\langle 110 \rangle$ ” region, the M_6 cubic parameter appears to nearly vanish while the δM_4 and M_4 parameters plateau to the approximate intermediate values 7/10 and 1/2, respectively. The values of the cubic parameters for this region are consistent with a $\langle 110 \rangle$ selection.

Having identified these three regions with their respective total magnetization orientation, we can now clarify the choice of the interaction parameter sets presented in Fig. 4: the two sets considered present a total magnetization vector reorientation as the temperature is lowered, exposing an intricate and rich phase diagram attributed to a thermal ObD selection of the Hamiltonian in Eq. (1). For completeness, we note that when $D/J = 0$, Eq. (1) is the ferromagnetic Heisenberg model, where the magnetization is isotropic due to rotational symmetry. In fact, in the region $-0.1 < D/J < 0.1$, the distribution $p(\hat{\mathbf{m}})$ does not acquire any distinctive pattern as the ones observed in Fig. 4, as the thermal selection is very weak and is not captured within the numerical accuracy of the current MC implementation applied in this work.

Appendix C: Calculation of the magnon self-energy

Here, we explicitly derive the expression for the magnon self-energy to $\mathcal{O}(S^0)$ using the imaginary-time Green’s function formalism. The three and four-magnon interaction vertices in Eqs. (19-20) are given by

$$Y_{\mathbf{k},\mathbf{q}}^{\mu\nu\lambda}(\hat{\mathbf{m}}) = i\sqrt{2}D\mathbf{d}_{\mu\nu} \cdot \mathbf{e}^- \left(\delta_{\nu\lambda} \cos(\mathbf{k} \cdot \mathbf{r}_{\mu\nu}) - \delta_{\mu\lambda} \cos(\mathbf{q} \cdot \mathbf{r}_{\mu\nu}) \right), \quad (\text{C1})$$

$$\begin{aligned} V_{\mathbf{k},\mathbf{q},\mathbf{Q}}^{\mu\nu\lambda\rho}(\hat{\mathbf{m}}) &= -2J(1 - \delta_{\mu\nu}) \left[\delta_{\mu\rho} \delta_{\nu\lambda} \cos(\mathbf{Q} \cdot \mathbf{r}_{\mu\nu}) \right. \\ &\quad \left. + \delta_{\mu\lambda} \delta_{\nu\rho} \cos((\mathbf{k} - \mathbf{q} + \mathbf{Q}) \cdot \mathbf{r}_{\mu\nu}) \right] \\ &\quad + 2(J - iD\mathbf{d}_{\mu\nu} \cdot \hat{\mathbf{m}})(1 - \delta_{\mu\rho}) \left[\delta_{\mu\nu} \delta_{\mu\lambda} \cos(\mathbf{k} \cdot \mathbf{r}_{\mu\rho}) \right. \\ &\quad \left. + \delta_{\lambda\rho} \delta_{\lambda\nu} \cos((\mathbf{k} + \mathbf{Q}) \cdot \mathbf{r}_{\mu\rho}) \right], \end{aligned} \quad (\text{C2})$$

where $\mathbf{e}^- \equiv \hat{\mathbf{e}}_1 - i\hat{\mathbf{e}}_2$.

We calculate the self-energy to $\mathcal{O}(S^0)$ by evaluating the diagrams depicted in Fig. 2 in the imaginary time formalism at finite temperature $T = 1/\beta$, and subsequently extrapolate to

zero temperature ($\beta \rightarrow \infty$). First, we express the interactions in terms of the operators $a_{q,\mu} = \sum_{\nu} U_{\mu,\nu}^{(\hat{m})}(\mathbf{q})b_{q,\nu}$ that diagonalize the linear spin-wave theory. Eqs. (19-20) become

$$\mathcal{H}_3^{(\hat{m})} = \frac{1}{2! \sqrt{N}} \sum_{kq} \sum_{\mu\nu\lambda} \left[T_{k,q}^{\mu\nu\lambda}(\hat{m}) b_{k,\mu}^{\dagger} b_{q,\nu}^{\dagger} b_{k+q,\lambda} + \text{H.c.} \right] \quad (\text{C3})$$

and

$$\mathcal{H}_4^{(\hat{m})} = \frac{1}{N(2!)^2} \sum_{kqQ} \sum_{\mu\nu\lambda\rho} W_{k,q,Q}^{\mu\nu\lambda\rho}(\hat{m}) b_{k+Q,\mu}^{\dagger} b_{q-Q,\nu}^{\dagger} b_{q,\lambda} b_{k,\rho}, \quad (\text{C4})$$

with the transformed interaction vertices defined as

$$T_{k,q}^{\mu\nu\lambda}(\hat{m}) = \sum_{\alpha\beta\gamma} \bar{U}_{\alpha\mu}^{(\hat{m})}(\mathbf{k}) \bar{U}_{\beta\nu}^{(\hat{m})}(\mathbf{q}) U_{\gamma\lambda}^{(\hat{m})}(\mathbf{k} + \mathbf{q}) Y_{k,q}^{\alpha\beta\gamma}(\hat{m}) \quad (\text{C5})$$

$$W_{k,q,Q}^{\mu\nu\lambda\rho}(\hat{m}) = \sum_{\alpha\beta\gamma\sigma} \left[\bar{U}_{\alpha\mu}^{(\hat{m})}(\mathbf{k} + \mathbf{Q}) \bar{U}_{\beta\nu}^{(\hat{m})}(\mathbf{q} - \mathbf{Q}) \times U_{\gamma\lambda}^{(\hat{m})}(\mathbf{q}) U_{\sigma\rho}^{(\hat{m})}(\mathbf{k}) V_{k,q,Q}^{\alpha\beta\gamma\sigma}(\hat{m}) \right]. \quad (\text{C6})$$

The bare imaginary-time Green's function in the diagonalized linear spin wave basis is given by

$$\mathcal{G}_{\alpha\beta}^{(\hat{m})}(\mathbf{k}, i\omega) = \frac{\delta_{\alpha\beta}}{-i\omega + S\omega_{\alpha,\mathbf{k}}^{(\hat{m})}}. \quad (\text{C7})$$

We decompose the imaginary-time self-energy into the sum of each of the diagram contributions in Fig. 2 as $\Sigma^{(\hat{m})} = \Sigma^a + \Sigma^b + \Sigma^c$.

In order of appearance, the diagrams are evaluated as

$$\Sigma_{\mu\nu}^a(\mathbf{k}, i\omega) = \frac{S}{2N\beta} \sum_{q,n} \sum_{\lambda\rho} \left[T_{q,k-q}^{\lambda\rho\mu}(\hat{m}) \bar{T}_{q,k-q}^{\lambda\rho\nu}(\hat{m}) \times \mathcal{G}_{\lambda\lambda}^{(\hat{m})}(\mathbf{q}, i\Omega_n) \mathcal{G}_{\rho\rho}^{(\hat{m})}(\mathbf{k} - \mathbf{q}, i\omega - i\Omega_n) \right], \quad (\text{C8})$$

$$\Sigma_{\mu\nu}^b(\mathbf{k}, i\omega) = \frac{S}{2N\beta} \sum_{q,n} \sum_{Q,n'} \sum_{\lambda\rho} \left[T_{k,Q}^{\nu\lambda\mu}(\hat{m}) \bar{T}_{q,Q}^{\rho\lambda\rho}(\hat{m}) \times \mathcal{G}_{\lambda\lambda}^{(\hat{m})}(\mathbf{Q}, i\Omega_{n'}) \mathcal{G}_{\rho\rho}^{(\hat{m})}(\mathbf{q}, i\Omega_n) \delta_{Q,0} \delta_{n',0} \right], \quad (\text{C9})$$

$$\Sigma_{\mu\nu}^c(\mathbf{k}, i\omega) = \frac{S}{2N\beta} \sum_{q,n} \sum_{\lambda} \left[\left(W_{k,q,q-k}^{\lambda\nu\lambda\mu}(\hat{m}) + W_{k,q,0}^{\nu\lambda\lambda\mu}(\hat{m}) \right) \times \mathcal{G}_{\lambda\lambda}^{(\hat{m})}(\mathbf{q}, i\Omega_n) \right], \quad (\text{C10})$$

where $\Omega_n = 2\pi n/\beta$ are the bosonic Matsubara frequencies. We can then evaluate each of the frequency summations and subsequently take the $\beta \rightarrow \infty$ limit as

$$\frac{1}{\beta} \sum_n \mathcal{G}_{\lambda\lambda}^{(\hat{m})}(\mathbf{q}, i\Omega_n) = n_B(S\omega_{\lambda,\mathbf{q}}^{(\hat{m})}) \xrightarrow{\beta \rightarrow \infty} 0, \quad (\text{C11})$$

and

$$\begin{aligned} & \frac{1}{\beta} \sum_n \mathcal{G}_{\lambda\lambda}^{(\hat{m})}(\mathbf{q}, i\Omega_n) \mathcal{G}_{\rho\rho}^{(\hat{m})}(\mathbf{k} - \mathbf{q}, i\omega - i\Omega_n) \\ &= \frac{n_B(S\omega_{\lambda,\mathbf{q}}^{(\hat{m})}) - n_B(i\omega - S\omega_{\rho,\mathbf{k}-\mathbf{q}}^{(\hat{m})})}{i\omega - S\omega_{\lambda,\mathbf{k}-\mathbf{q}}^{(\hat{m})} - S\omega_{\rho,\mathbf{q}}^{(\hat{m})}} \\ & \xrightarrow{\beta \rightarrow \infty} \frac{1}{i\omega - S\omega_{\lambda,\mathbf{k}-\mathbf{q}}^{(\hat{m})} - S\omega_{\rho,\mathbf{q}}^{(\hat{m})}}. \end{aligned} \quad (\text{C12})$$

It follows that $\Sigma^b = \Sigma^c = 0$, and

$$\Sigma_{\mu\nu}^a(\mathbf{k}, i\omega) = \frac{S}{2N} \sum_q \sum_{\lambda\rho} \frac{(T_{q,k-q}^{\lambda\rho\mu}(\hat{m})) (T_{q,k-q}^{\lambda\rho\nu}(\hat{m}))^*}{i\omega - S\omega_{\lambda,\mathbf{k}-\mathbf{q}}^{(\hat{m})} - S\omega_{\rho,\mathbf{q}}^{(\hat{m})}}. \quad (\text{C13})$$

The retarded self-energy is then obtained by analytic continuation which, making the substitution $i\omega \rightarrow \omega + i0^+$, leads to Eq. (23).

-
- [1] J. Villain, Insulating spin glasses, *Zeitschrift für Physik B Condensed Matter* **33**, 31 (1979).
 - [2] R. Moessner and J. T. Chalker, Low-temperature properties of classical geometrically frustrated antiferromagnets, *Phys. Rev. B* **58**, 12049 (1998).
 - [3] B. Canals and C. Lacroix, Pyrochlore antiferromagnet: A three-dimensional quantum spin liquid, *Phys. Rev. Lett.* **80**, 2933 (1998).
 - [4] A. Kitaev, Anyons in an exactly solved model and beyond, *Annals of Physics January Special Issue*, **321**, 2 (2006).
 - [5] L. Balents, Spin liquids in frustrated magnets, *Nature* **464**, 199

(2010).

- [6] M. J. P. Gingras and P. A. McClarty, Quantum spin ice: A search for gapless quantum spin liquids in pyrochlore magnets, *Reports on Progress in Physics* **77**, 056501 (2014).
- [7] T. Imai and Y. S. Lee, Do quantum spin liquids exist?, *Physics Today* **69**, 30 (2016).
- [8] L. Savary and L. Balents, Quantum spin liquids: A review, *Reports on Progress in Physics* **80**, 016502 (2017).
- [9] J. Knolle and R. Moessner, A field guide to spin liquids, *Annual Review of Condensed Matter Physics* **10**, 451 (2019).
- [10] The term order-by-disorder may be confusing in this context,

and should really be thought of as “order-by-fluctuations”.

- [11] J. Villain, R. Bidaux, J.-P. Carton, and R. Conte, Order as an effect of disorder, *Journal de Physique* **41**, 1263 (1980).
- [12] E. Belorizky, R. Casalegno, and J. J. Niez, Calculation of the Spin Wave Energy Gap at $k = 0$ for a Simple Cubic Ferromagnet with Anisotropic Exchange Interactions, *physica status solidi (b)* **102**, 365 (1980).
- [13] P. Chandra and B. Douçot, Possible spin-liquid state at large S for the frustrated square Heisenberg lattice, *Phys. Rev. B* **38**, 9335 (1988).
- [14] C. L. Henley, Ordering due to disorder in a frustrated vector antiferromagnet, *Phys. Rev. Lett* **62**, 2056 (1989).
- [15] S. Prakash and C. L. Henley, Ordering due to disorder in dipolar magnets on two-dimensional lattices, *Phys. Rev. B* **42**, 6574 (1990).
- [16] C. L. Henley, Ordering by disorder: Ground-state selection in fcc vector antiferromagnets, *Journal of Applied Physics* **61**, 3962 (1987).
- [17] C. Kittel, *Quantum Theory of Solids*, 2nd ed. (Wiley, New York, NY, 1991).
- [18] S. T. Bramwell, M. J. P. Gingras, and J. N. Reimers, Order by disorder in an anisotropic pyrochlore lattice antiferromagnet, *Journal of Applied Physics* **75**, 5523 (1994).
- [19] R. R. Sobral and C. Lacroix, Order by disorder in the pyrochlore antiferromagnets, *Solid State Communications* **103**, 407 (1997).
- [20] J. Oitmaa, R. R. P. Singh, B. Javanparast, A. G. R. Day, B. V. Bagheri, and M. J. P. Gingras, Phase transition and thermal order-by-disorder in the pyrochlore antiferromagnet $\text{Er}_2\text{Ti}_2\text{O}_7$: A high-temperature series expansion study, *Phys. Rev. B* **88**, 220404 (2013).
- [21] J. N. Reimers and A. J. Berlinsky, Order by disorder in the classical Heisenberg kagomé Antiferromagnet, *Phys. Rev. B* **48**, 9539 (1993).
- [22] M. Elhajal, B. Canals, R. Sunyer, and C. Lacroix, Ordering in the pyrochlore antiferromagnet due to Dzyaloshinsky-Moriya interactions, *Phys. Rev. B* **71**, 094420 (2005).
- [23] D. Bergman, J. Alicea, E. Gull, S. Trebst, and L. Balents, Order-by-disorder and spiral spin-liquid in frustrated diamond-lattice antiferromagnets, *Nature Physics* **3**, 487 (2007).
- [24] G.-W. Chern, Pyrochlore antiferromagnet with antisymmetric exchange interactions: critical behavior and order from disorder, [arXiv:1008.3038 \[cond-mat.str-el\]](https://arxiv.org/abs/1008.3038) (2010).
- [25] M. E. Zhitomirsky, P. C. W. Holdsworth, and R. Moessner, Nature of finite-temperature transition in anisotropic pyrochlore $\text{Er}_2\text{Ti}_2\text{O}_7$, *Phys. Rev. B* **89**, 140403 (2014).
- [26] P. A. McClarty, P. Stasiak, and M. J. P. Gingras, Order-by-disorder in the XY pyrochlore antiferromagnet, *Phys. Rev. B* **89**, 024425 (2014).
- [27] J. R. Tessman, Magnetic Anisotropy at 0°K , *Phys. Rev* **96**, 1192 (1954).
- [28] E. F. Shender, Antiferromagnetic garnets with fluctuonally interacting sublattices, *Sov. Phys. JETP* **56**, 178 (1982).
- [29] K. Kubo and T. Kishi, Ordering Due to Quantum Fluctuations in the Frustrated Heisenberg Model, *Journal of the Physical Society of Japan* **60**, 567 (1991).
- [30] S. Sachdev, Kagomé and triangular-lattice Heisenberg antiferromagnets: Ordering from quantum fluctuations and quantum-disordered ground states with unconfined bosonic spinons, *Phys. Rev. B* **45**, 12377 (1992).
- [31] A. Chubukov, Order from Disorder in a Kagomé Antiferromagnet, *Phys. Rev. Lett* **69**, 832 (1992).
- [32] C. L. Henley, Selection by Quantum Fluctuations of Dipolar Order in a Diamond Lattice, *Phys. Rev. Lett* **73**, 2788 (1994).
- [33] P. Lecheminant, B. Bernu, C. Lhuillier, and L. Pierre, $J_1 - J_2$ quantum Heisenberg antiferromagnet on the triangular lattice: A group-symmetry analysis of order by disorder, *Phys. Rev. B* **52**, 6647 (1995).
- [34] J. D. M. Champion, M. J. Harris, P. C. W. Holdsworth, A. S. Wills, G. Balakrishnan, S. T. Bramwell, E. Čížmár, T. Fennell, J. S. Gardner, J. Lago, D. F. McMorrow, M. Orendáč, A. Orendáčová, D. M. Paul, R. I. Smith, M. T. F. Telling, and A. Wildes, $\text{Er}_2\text{Ti}_2\text{O}_7$: Evidence of quantum order by disorder in a frustrated antiferromagnet, *Phys. Rev. B* **68**, 020401 (2003).
- [35] G. Baskaran, D. Sen, and R. Shankar, Spin- S Kitaev model: Classical ground states, order from disorder, and exact correlation functions, *Phys. Rev. B* **78**, 115116 (2008).
- [36] J.-S. Bernier, M. J. Lawler, and Y. B. Kim, Quantum Order by Disorder in Frustrated Diamond Lattice Antiferromagnets, *Phys. Rev. Lett* **101**, 047201 (2008).
- [37] A. Mulder, R. Ganesh, L. Capriotti, and A. Paramekanti, Spiral order by disorder and lattice nematic order in a frustrated Heisenberg antiferromagnet on the honeycomb lattice, *Phys. Rev. B* **81**, 214419 (2010).
- [38] L. Savary, K. A. Ross, B. D. Gaulin, J. P. C. Ruff, and L. Balents, Order by Quantum Disorder in $\text{Er}_2\text{Ti}_2\text{O}_7$, *Phys. Rev. Lett* **109**, 167201 (2012).
- [39] M. E. Zhitomirsky, M. V. Gvozdikova, P. C. W. Holdsworth, and R. Moessner, Quantum Order by Disorder and Accidental Soft Mode in $\text{Er}_2\text{Ti}_2\text{O}_7$, *Phys. Rev. Lett* **109**, 077204 (2012).
- [40] A. L. Chernyshev and M. E. Zhitomirsky, Quantum Selection of Order in an XXZ Antiferromagnet on a Kagome Lattice, *Phys. Rev. Lett.* **113**, 237202 (2014).
- [41] I. Rousochatzakis, J. Reuther, R. Thomale, S. Rachel, and N. B. Perkins, Phase Diagram and Quantum Order by Disorder in the Kitaev $K_1 - K_2$ Honeycomb Magnet, *Phys. Rev. X* **5**, 041035 (2015).
- [42] B. Placke, R. Moessner, and O. Benton, Hierarchy of energy scales and field-tunable order by disorder in dipolar-octupolar pyrochlores, *Phys. Rev. B* **102**, 245102 (2020).
- [43] G. Chen and X. Wang, Electron quasi-itinerancy intertwined with quantum order by disorder in pyrochlore iridate magnetism, *Phys. Rev. Res.* **2**, 043273 (2020).
- [44] C. Liu, C.-J. Huang, and G. Chen, Intrinsic quantum ising model on a triangular lattice magnet TmMgGao_4 , *Phys. Rev. Res.* **2**, 043013 (2020).
- [45] S. Khatua, S. Srinivasan, and R. Ganesh, State selection in frustrated magnets, *Phys. Rev. B* **103**, 174412 (2021).
- [46] S. Lee, E. K.-H. Lee, A. Paramekanti, and Y. B. Kim, Order-by-disorder and magnetic field response in the heisenberg-kitaev model on a hyperhoneycomb lattice, *Phys. Rev. B* **89**, 014424 (2014).
- [47] B. Danu, G. Nambiar, and R. Ganesh, Extended degeneracy and order by disorder in the square lattice $J_1 - J_2 - J_3$ model, *Phys. Rev. B* **94**, 094438 (2016).
- [48] R. Schick, T. Ziman, and M. E. Zhitomirsky, Quantum versus thermal fluctuations in the fcc antiferromagnet: Alternative routes to order by disorder, *Phys. Rev. B* **102**, 220405 (2020).
- [49] V. Noculak, D. Lozano-Gómez, J. Oitmaa, R. R. P. Singh, Y. Iqbal, M. J. P. Gingras, and J. Reuther, Classical and quantum phases of the pyrochlore $S = \frac{1}{2}$ magnet with Heisenberg and Dzyaloshinskii-Moriya interactions, *Phys. Rev. B* **107**, 214414 (2023).
- [50] Y. V. Fyodorov and E. F. Shender, Random-field effects in antiferromagnets with classically degenerate ground states, *Journal of Physics: Condensed Matter* **3**, 9123 (1991).
- [51] L. Savary, E. Gull, S. Trebst, J. Alicea, D. Bergman, and L. Balents, Impurity effects in highly frustrated diamond-lattice antiferromagnets, *Phys. Rev. B* **84**, 064438 (2011).

- [52] V. S. Maryasin and M. E. Zhitomirsky, Triangular Antiferromagnet with Nonmagnetic Impurities, *Phys. Rev. Lett.* **111**, 247201 (2013).
- [53] V. S. Maryasin and M. E. Zhitomirsky, Collective impurity effects in the heisenberg triangular antiferromagnet, *Journal of Physics: Conference Series* **592**, 012112 (2015).
- [54] A. I. Smirnov, T. A. Soldatov, O. A. Petrenko, A. Takata, T. Kida, M. Hagiwara, A. Y. Shapiro, and M. E. Zhitomirsky, Order by Quenched Disorder in the Model Triangular Antiferromagnet $\text{RbFe}(\text{MoO}_4)_2$, *Phys. Rev. Lett.* **119**, 047204 (2017).
- [55] E. C. Andrade, J. A. Hoyos, S. Rachel, and M. Vojta, Cluster-Glass Phase in Pyrochlore XY Antiferromagnets with Quenched Disorder, *Phys. Rev. Lett.* **120**, 097204 (2018).
- [56] K. A. Ross, Y. Qiu, J. R. D. Copley, H. A. Dabkowska, and B. D. Gaulin, Order by Disorder Spin Wave Gap in the XY Pyrochlore Magnet $\text{Er}_2\text{Ti}_2\text{O}_7$, *Phys. Rev. Lett.* **112**, 057201 (2014).
- [57] S. Petit, J. Robert, S. Guitteny, P. Bonville, C. Decorse, J. Ollivier, H. Mutka, M. J. P. Gingras, and I. Mirebeau, Order by disorder or energetic selection of the ground state in the XY pyrochlore antiferromagnet $\text{Er}_2\text{Ti}_2\text{O}_7$: An inelastic neutron scattering study, *Phys. Rev. B* **90**, 060410 (2014).
- [58] Although selection, at least in part, due to virtual crystal field fluctuations has not been ruled out [57, 69, 98].
- [59] M. Elliot, P. A. McClarty, D. Prabhakaran, R. D. Johnson, H. C. Walker, P. Manuel, and R. Coldea, Order-by-Disorder from Bond-Dependent Exchange and Intensity Signature of Nodal Quasiparticles in a Honeycomb Cobaltate, *Nature Communications* **12**, 3936 (2021).
- [60] Y. J. Kim, A. Aharony, R. J. Birgeneau, F. C. Chou, O. Entin-Wohlman, R. W. Erwin, M. Greven, A. B. Harris, M. A. Kastner, I. Y. Korenblit, Y. S. Lee, and G. Shirane, Ordering due to Quantum Fluctuations in $\text{Sr}_2\text{Cu}_3\text{O}_4\text{Cl}_2$, *Phys. Rev. Lett.* **83**, 852 (1999).
- [61] T. Brueckel, B. Dorner, A. G. Gukasov, V. P. Plakhty, W. Prandl, E. F. Shender, and O. P. Smirnow, Dynamical interaction of antiferromagnetic subsystems: a neutron scattering study of the spinwave spectrum of the garnet $\text{Fe}_2\text{Ca}_3(\text{GeO}_4)_3$, *Zeitschrift für Physik B Condensed Matter* **72**, 477 (1988).
- [62] C. L. Sarkis, J. G. Rau, L. D. Sanjeeva, M. Powell, J. Kolis, J. Marbey, S. Hill, J. A. Rodriguez-Rivera, H. S. Nair, D. R. Yahne, S. Säubert, M. J. P. Gingras, and K. A. Ross, Unraveling competing microscopic interactions at a phase boundary: A single-crystal study of the metastable antiferromagnetic pyrochlore $\text{Yb}_2\text{Ge}_2\text{O}_7$, *Phys. Rev. B* **102**, 134418 (2020).
- [63] In this work we do not consider the possibility of antiferromagnetic $J < 0$ [49].
- [64] T. Moriya, Anisotropic Superexchange Interaction and Weak Ferromagnetism, *Phys. Rev.* **120**, 91 (1960).
- [65] H. Yan, O. Benton, L. Jaubert, and N. Shannon, Theory of multiple-phase competition in pyrochlore magnets with anisotropic exchange with application to $\text{Yb}_2\text{Ti}_2\text{O}_7$, $\text{Er}_2\text{Ti}_2\text{O}_7$, and $\text{Er}_2\text{Sn}_2\text{O}_7$, *Phys. Rev. B* **95**, 094422 (2017).
- [66] There is an exception to this statement when $D = 0$. In this case, Eq. (1) is simply the ferromagnetic Heisenberg model which has an exact $O(3)$ symmetry, and therefore the ground state degeneracy is no longer accidental.
- [67] D. Coffey, T. M. Rice, and F. C. Zhang, Dzyaloshinskii-moriya interaction in the cuprates, *Phys. Rev. B* **44**, 10112 (1991).
- [68] K. Riedl, D. Guterding, H. O. Jeschke, M. J. P. Gingras, and R. Valentí, Ab Initio Determination of Spin Hamiltonians with Anisotropic Exchange Interactions: The Case of the Pyrochlore Ferromagnet $\text{Lu}_2\text{V}_2\text{O}_7$, *Phys. Rev. B* **94**, 014410 (2016).
- [69] P. A. McClarty, S. H. Curnoe, and M. J. P. Gingras, Energetic selection of ordered states in a model of the $\text{Er}_2\text{Ti}_2\text{O}_7$ frustrated pyrochlore XY antiferromagnet, *Journal of Physics: Conference Series* **145**, 012032 (2009).
- [70] K. A. Ross, L. Savary, B. D. Gaulin, and L. Balents, Quantum excitations in quantum spin ice, *Phys. Rev. X* **1**, 021002 (2011).
- [71] Here, we refer to the Kitaev interaction for the pyrochlore lattice in the same way that it is used in Ref. [72]. The collinear ferromagnet is still the classical ground state configuration when a small but non-zero Kitaev interaction is present. However, the ferromagnetic product state will no longer be an exact eigenstate of the quantum Hamiltonian. This, in turn, will generate zero-point fluctuations proportional to K , and there will be quantum ObD present in addition to thermal ObD, as is expected in a typical quantum ObD scenario.
- [72] J. G. Rau and M. J. P. Gingras, Frustration and anisotropic exchange in ytterbium magnets with edge-shared octahedra, *Phys. Rev. B* **98**, 054408 (2018).
- [73] J. G. Rau and M. J. P. Gingras, Frustrated Quantum Rare-Earth Pyrochlores, *Annual Review of Condensed Matter Physics* **10**, 357 (2019).
- [74] S.-i. Shamoto, T. Nakano, Y. Nozue, and T. Kajitani, Substitution Effects on Ferromagnetic Mott Insulator $\text{Lu}_2\text{V}_2\text{O}_7$, *Journal of Physics and Chemistry of Solids* **63**, 1047 (2002).
- [75] A. Ali Biswas and Y. Jana, Crystal-Field, Exchange Interactions and Magnetism in Pyrochlore Ferromagnet $\text{R}_2\text{V}_2\text{O}_7$ ($\text{R}^{3+}=\text{Y}, \text{Lu}$), *Journal of Magnetism and Magnetic Materials* **329**, 118 (2013).
- [76] D. V. Nazipov, A. E. Nikiforov, and V. A. Chernyshev, Exchange interaction in pyrochlore vanadates $\text{Lu}_2\text{V}_2\text{O}_7$ and $\text{Y}_2\text{V}_2\text{O}_7$: Ab initio approach, *Physics of the Solid State* **58**, 1989 (2016).
- [77] D. V. Nazipov, A. E. Nikiforov, and V. A. Chernyshev, Structure, lattice dynamics, and exchange interaction in $\text{Lu}_2\text{V}_2\text{O}_7$, $\text{Y}_2\text{V}_2\text{O}_7$: an ab initio approach, *Optics and Spectroscopy* **121**, 544 (2016).
- [78] Y. Onose, T. Ideue, H. Katsura, Y. Shiomi, N. Nagaosa, and Y. Tokura, Observation of the Magnon Hall Effect, *Science* **329**, 297 (2010).
- [79] M. Mena, R. S. Perry, T. G. Perring, M. D. Le, S. Guerrero, M. Storni, D. T. Adroja, C. Rüegg, and D. F. McMorrow, Spin-Wave Spectrum of the Quantum Ferromagnet on the Pyrochlore Lattice $\text{Lu}_2\text{V}_2\text{O}_7$, *Phys. Rev. Lett.* **113**, 047202 (2014).
- [80] J. D. Alzate-Cardona, D. Sabogal-Suárez, R. F. L. Evans, and E. Restrepo-Parra, Optimal phase space sampling for Monte Carlo simulations of Heisenberg spin systems, *Journal of Physics: Condensed Matter* **31**, 095802 (2019).
- [81] K. Binder and D. W. Heermann, *Monte Carlo Simulation in Statistical Physics: An Introduction* (Springer Science & Business Media, 2010).
- [82] M. Creutz, Overrelaxation and Monte Carlo simulation, *Phys. Rev. D* **36**, 515 (1987).
- [83] J. P. Bouchaud and P. G. Zerah, Dipolar ferromagnetism: A Monte Carlo study, *Phys. Rev. B* **47**, 9095 (1993).
- [84] P. M. Chaikin and T. C. Lubensky, *Principles of Condensed Matter Physics* (Cambridge University Press, 2000).
- [85] T. Holstein and H. Primakoff, Field Dependence of the Intrinsic Domain Magnetization of a Ferromagnet, *Phys. Rev.* **58**, 1098 (1940).
- [86] J. G. Rau, R. Moessner, and P. A. McClarty, Magnon interactions in the frustrated pyrochlore ferromagnet $\text{Yb}_2\text{Ti}_2\text{O}_7$, *Phys. Rev. B* **100**, 104423 (2019).
- [87] M. Mourigal, W. T. Fuhrman, A. L. Chernyshev, and M. E. Zhitomirsky, Dynamical structure factor of the triangular-lattice antiferromagnet, *Phys. Rev. B* **88**, 094407 (2013).
- [88] G. D. Mahan, *Many-Particle Physics*, 3rd ed. (Springer, New York, NY, 2000).
- [89] D. Lozano-Gómez, V. Noculak, J. Oitmaa, R. R. P. Singh,

- Y. Iqbal, J. Reuther, and M. J. P. Gingras, Competing Gauge Fields and Entropically-Driven Spin Liquid to Spin Liquid Transition in non-kramers Pyrochlores, [arXiv:2310.16682 \[cond-mat.str-el\]](https://arxiv.org/abs/2310.16682) (2023).
- [90] S. Weinberg, Approximate Symmetries and Pseudo-Goldstone Bosons, *Phys. Rev. Lett* **29**, 1698 (1972).
- [91] C. Burgess, Goldstone and pseudo-Goldstone bosons in nuclear, particle and condensed-matter physics, *Physics Reports* **330**, 193 (2000).
- [92] J. G. Rau, P. A. McClarty, and R. Moessner, Pseudo-Goldstone Gaps and Order-by-Quantum Disorder in Frustrated Magnets, *Phys. Rev. Lett* **121**, 237201 (2018).
- [93] S. Khatua, M. J. P. Gingras, and J. G. Rau, Pseudo-Goldstone Modes and Dynamical Gap Generation from Order by Thermal Disorder, *Phys. Rev. Lett* **130**, 266702 (2023).
- [94] M. E. Zhitomirsky and A. L. Chernyshev, *Colloquium* : Spontaneous magnon decays, *Reviews of Modern Physics* **85**, 219 (2013).
- [95] A. Aharony, Critical Behavior of Anisotropic Cubic Systems, *Phys. Rev. B* **8**, 4270 (1973).
- [96] M. Caselle and M. Hasenbusch, The stability of the $O(N)$ invariant fixed point in three dimensions, *Journal of Physics A: Mathematical and General* **31**, 4603 (1998).
- [97] L. T. Adzhemyan, E. V. Ivanova, M. V. Kompaniets, A. Kudlis, and A. I. Sokolov, Six-loop ε expansion study of three-dimensional n -vector model with cubic anisotropy, *Nuclear Physics B* **940**, 332 (2019).
- [98] J. G. Rau, S. Petit, and M. J. P. Gingras, Order by virtual crystal field fluctuations in pyrochlore XY antiferromagnets, *Phys. Rev. B* **93**, 184408 (2016).